frontiers | Frontiers in Energy Research

ORIGINAL RESEARCH
published: 30 June 2022
doi: 10.3389/fenrg.2022.874467

Impedance Modeling and Stability-Oriented Parameter Optimization of Isolated Dual Active Bridge-Based Two-Stage AC-DC-DC Converter

Fan Feng[1], Jingyang Fang[2], Ujjal Manandhar[3], Hoay Beng Gooi[3] and Liguo Wang[1]**

[1]School of Marine Engineering and Technology, Sun Yat-sen University, Zhuhai, China, [2]School of Control Science and Engineering, Shandong University, Jinan, China, [3]School of Electrical and Electronic Engineering, Nanyang Technological University, Singapore

The isolated dual active bridge (DAB)-based two-stage AC-DC-DC converters have been widely applied in grid-connected power electronics systems. However, the impedance interactions between the DAB converter and the AC-DC rectifier can cause instability problems to the two-stage converter systems. The accurate terminal impedance characteristics of the DAB converters are still not clear due to the high frequency ac conversion stage. This makes it difficult to assess the impacts of the DAB circuit parameters on the stability of the two-stage converters. To address these issues, the impedance models of the DAB converters are originally derived in this paper. Based on the developed impedance models, the stability of the DAB-based two-stage AC-DC-DC converters is analyzed. The impacts of the DAB converter circuit parameters on the stability of the two-stage AC-DC-DC converters are comprehensively revealed by the Bode and Nyquist plots. The analysis results offer instructive implications to finetune the design rules of the DAB converters. The conclusions are validated by comprehensive simulation and experimental results.

Keywords: dual active bridge, impedance modeling, stability analysis, two-stage converter, parameter optimization

OPEN ACCESS

Edited by:
Sudhakar Babu Thanikanti, Chaitanya Bharathi Institute of Technology, India

Reviewed by:
Ning Gao, Shanghai Maritime University, China
Subhendu Bikash Santra, KIIT University, India

****Correspondence:***
Jingyang Fang
jingyangfang@sdu.edu.cn
Liguo Wang
wanglg7@mail.sysu.edu.cn

Specialty section:
This article was submitted to Smart Grids, a section of the journal Frontiers in Energy Research

Received: *12 February 2022*
Accepted: *10 June 2022*
Published: *30 June 2022*

Citation:
Feng F, Fang J, Manandhar U, Gooi HB and Wang L (2022) Impedance Modeling and Stability-Oriented Parameter Optimization of Isolated Dual Active Bridge-Based Two-Stage AC-DC-DC Converter. Front. Energy Res. 10:874467. doi: 10.3389/fenrg.2022.874467

1 INTRODUCTION

In order to connect various DC energy storage sources, such as the batteries and supercapacitors, to the AC utility grids, one of the most common topologies is the two-stage AC-DC-DC converter which consists of an isolated DC-DC conversion stage and an AC-DC stage (Blaabjerg et al., 2004; Wu et al., 2015; Feng et al., 2020). Among the bidirectional DC-DC converter topologies, the dual active bridge (DAB) converter is becoming more and more popular because of its advantages on the high-power density, galvanic isolation, and soft switching (Krismer and Kolar 2009; Roggia et al., 2013; Ye et al., 2017). **Figure 1** shows the DAB-based two-stage AC-DC-DC converter. Literature (Wu et al., 2018) proposed the cooperative triple phase shift (CTPS) control is proposed to eliminate the dual-side flow back currents and reduce the current stress of the DAB converter. The CTPS-based DAB converter has a great potential for being used as the interface converter for the energy storage. Therefore, it is also applied in the two-stage AC-DC-DC converter in this paper.

However, it is found that this two-stage converter has instability issues. Although the DAB converter and the AC-DC rectifier are stable individually, the instable problem may occur when they are cascaded

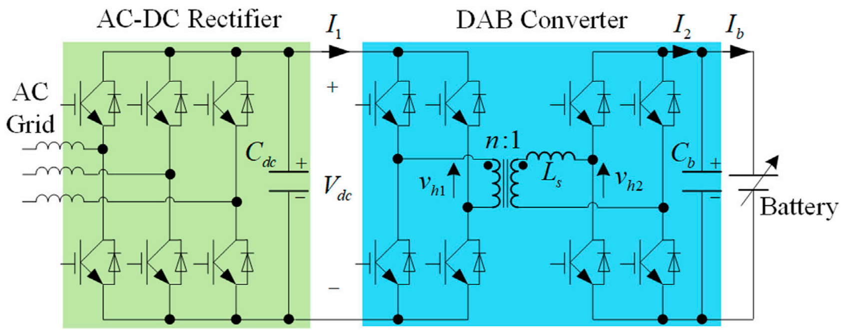

FIGURE 1 | Topology of the isolated two-stage AC-DC-DC converter.

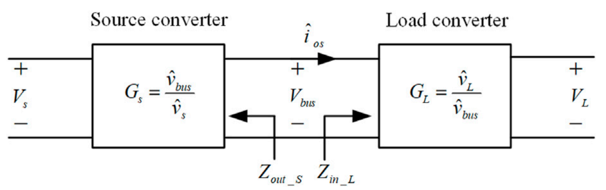

FIGURE 2 | Simplified representation of a two-stage converter.

together. Similar problems have also been reported in other two-stage systems (Radwan and Mohamed 2012; Wu et al., 2012; Liu et al., 2014; Wen et al., 2015). Driven by this issue, a lot of efforts have been made to investigate the stability criterion of the two-stage systems. The concept of the impedance-based stability criterion is first proposed in Literature Middlebrook and Cuk (1976), and later becomes the base for the stability analysis of cascaded systems (Sun 2011; Zhang et al., 2015). A general representation of a two-stage cascaded converter configuration is shown in **Figure 2**. The stability of the two-stage converter depends on the minor loop gain T_m, expressed as the ratio of the source converter output impedance Z_{out_S} to the load converter input impedance Z_{in_L}. If the impedance ratio T_m satisfies the Nyquist criterion, the two-stage converter will be stable.

Hence, to analyze the stability of the two-stage converter, it is necessary to derive the impedance models of the AC-DC rectifier and the DAB converter. The impedance model of AC-DC rectifier has been well established. However, the high frequency ac conversion stage brings difficulties to the model generation of the DAB converter. The reduced-order impedance models are derived in Literature (Tian et al., 2016; Tian et al., 2016), based on the "small-ripple" assumption. Since the dc average of the transformer current over a switching period is 0, the dynamics of the transformer current are neglected, thus leading to the sacrifice of accuracy. A full-order discrete-time model, which can obtain higher accuracy compared to the reduced-order model, is developed in Literature Zhao et al. (2010). However, for control design, the continuous model is more desirable. Based on the generalized averaging method, a full-order continuous-time model of the single-phase shift (SPS) modulated DAB converter is proposed and verified to be more accurate than the reduced order models at dc and low frequency (Qin and Kimball 2012). But the model is not extended to the derivation of the DAB converter input or output impedances. In Literature (Mueller and Kimball 2017), the closed-loop impedance of the SPS-DAB converter is calculated based on the Extra Element Theorem with a dummy controller. However, the derivation process is cumbersome and time-consuming for practical use. So far, the existing impedance models are derived from SPS-DAB converters and are not suitable for CTPS-DAB converters. Since the CTPS modulation is drawing increasing attention among the DAB converter applications, the impedance model of the CTPS-based DAB converters should be developed. Moreover, in previous applications, the design of the DAB converter circuit parameters is focused on the steady and dynamic performance (Tan et al., 2012). The influences of the circuit parameters on the stability of the two-stage converter have not been studied yet.

To fill up the gap, the full-order small signal impedance model of the CTPS-based DAB converter is originally derived in this paper. The developed impedance model is used to analyze the stability of the two-stage converter and the influences of the circuit parameters on the stability. Furthermore, the design of the DAB circuit parameters is revisited. The optimization guideline of the DAB circuit parameters is proposed to improve the stability of the two-stage converter.

The rest of this paper is organized as follows. The operation mechanism of the CTPS based DAB converter is analyzed in **Section 2**. And the small signal impedance models of the two-stage converter are derived in **Section 3**. The stability of the system and the effects of the filter capacitances are analyzed in **Section 4**. The simulation and hardware-in-the-loop (HIL) experimental results are presented in **Section 5** to verify the theoretical analysis. And **Section 6** gives the conclusions of this work.

2 PRELIMINARY: OPERATION PRINCIPLE AND STABILITY ASSESSMENT OF TWO-STAGE CONVERTERS

2.1 Operation Principle of CTPS-DAB Converters

The phase-shift modulation methods are the most widely used to regulate the power transferred in the DAB converters. It has been verified in Literature Wu et al. (2018) that the CTPS modulation

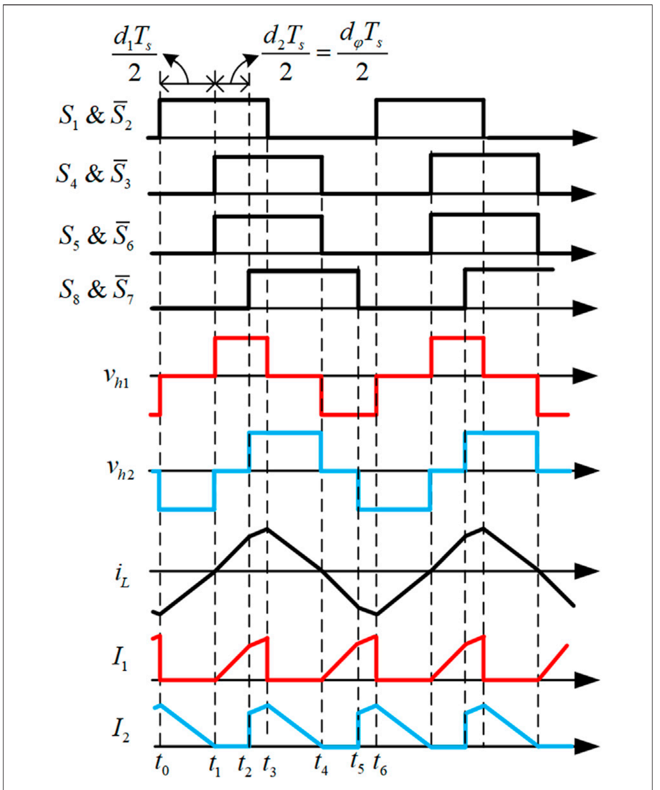

FIGURE 3 | Operating waveforms of the CTPS based DAB converter.

can eliminate the dual side flow back currents in the DAB converter and achieve better current characteristics, including the inductor current stress and RMS value. The CTPS-DAB converter is more efficient and reliable compared to other traditional phase-shift control methods. Therefore, the CTPS modulation is applied to the DAB-based two-stage converter in this paper. For the purpose of impedance modeling derivation, the relationship of the three control degrees, i.e., the phase-shift ratios, is given here. The details of the CTPS operation principle is omitted due to space limit but can be found in Literature Wu et al. (2018).

Figure 3 depicts the typical operation waveforms of CTPS-DAB converter. S_1–S_8 are the driving signals for the switches of the DAB converter. i_L is the inductor current. I_1 and I_2 are the input and output current of the DAB converter, respectively. v_{h1} and v_{h2} are the output voltages of the two H-bridges on the primary and secondary side of the transformer, respectively. T_s is the switching cycle of the DAB converter. d_φ is the phase-shift ratio between v_{h1} and v_{h2}. d_1 and d_2 are the phase-shift ratios of both primary and secondary H-bridges. All the time points t_1–t_6 can be found in **Table 1**. The driving signals S_4 or S_8 is reversed only when the I_1 or I_2 is zero. Thus, the polarities of v_{h1} and v_{h2} can be consistent with that of i_L. To meet this requirement, the total increment of i_L should be zero during half of a switching cycle, which can be expressed as in **Eq. 1**. And this constraint can be further simplified as in **Eq. 2**.

TABLE 1 | Mathematical expression of each time point.

Time point	Value	Time point	Value
t_0	0	t_1	$d_1\frac{T_s}{2}$
t_2	$(d_1+d_2)\frac{T_s}{2}$	t_3	$\frac{T_s}{2}$
t_4	$(1+d_1)\frac{T_s}{2}$	t_5	$(1+d_1+d_2)\frac{T_s}{2}$
t_6	T_s		

$$\left[1-d_2-\left(1-d_1-d_\varphi\right)\right]\frac{T_s}{2}\frac{v_c}{L_s}=d_\varphi\frac{T_s}{2}\frac{v_{dc}}{nL_s}+\left(1-d_1-d_\varphi\right)\frac{T_s}{2}\frac{v_{dc}-nv_c}{nL_s} \tag{1}$$

$$d_2=1+k(d_1-1) \tag{2}$$

where $k=nv_{dc}/v_c$; v_{dc} is the DC bus voltage; v_c is the voltage across the capacitance C_b; n is the turns ratio of the transformer; L_s is the inductance.

The outer phase shift ratio d_φ should be equal to d_2 to keep the same polarity of v_{h1} and v_{h2}, namely

$$d_\varphi=d_2 \tag{3}$$

2.2 Stability Analysis of Two-Stage Converters

According to Literature Zhang et al. (2015), the stability of the two-stage converter relies on the minor loop gain T_m, which is organized as the ratio of the voltage-controlled converter's output impedance to the current-controlled converter's input impedance.

Figure 4 shows the schematic and the control system block diagram of the two-stage AC-DC-DC converter, which is used to connect a battery to the utility grid. Between the DAB converter and the AC-DC rectifier, a DC-bus capacitor C_{dc} is used to smooth the DC-bus voltage ripple. The control of the two-stage AC-DC-DC converter can be split into two parts: the DC-DC conversion stage and the AC-DC conversion stage. The AC-DC rectifier is responsible for maintaining the DC bus voltage V_{dc} constant and realizing the grid current closed-loop control. The DAB converter closes the control loop regulating the battery charging current I_b. It should be noted that the control strategy of the two-stage converter keeps the same in bidirectional operation. From **Figure 4**, T_m can be calculated as:

$$T_m=\frac{Z_{o\_rec}}{Z_{in\_DAB}} \tag{4}$$

where Z_{o_rec} is the output impedance of the DC-AC rectifier and Z_{in_DAB} is the input impedance of the DAB converter.

The stability analysis of the two-stage converter therefore relies on the model-based determinations of the required impedances in **Eq. 4**. According to Literature (Tian et al., 2016), two-stage converters have instable problems only when the power is transferred from the voltage-controlled sub-

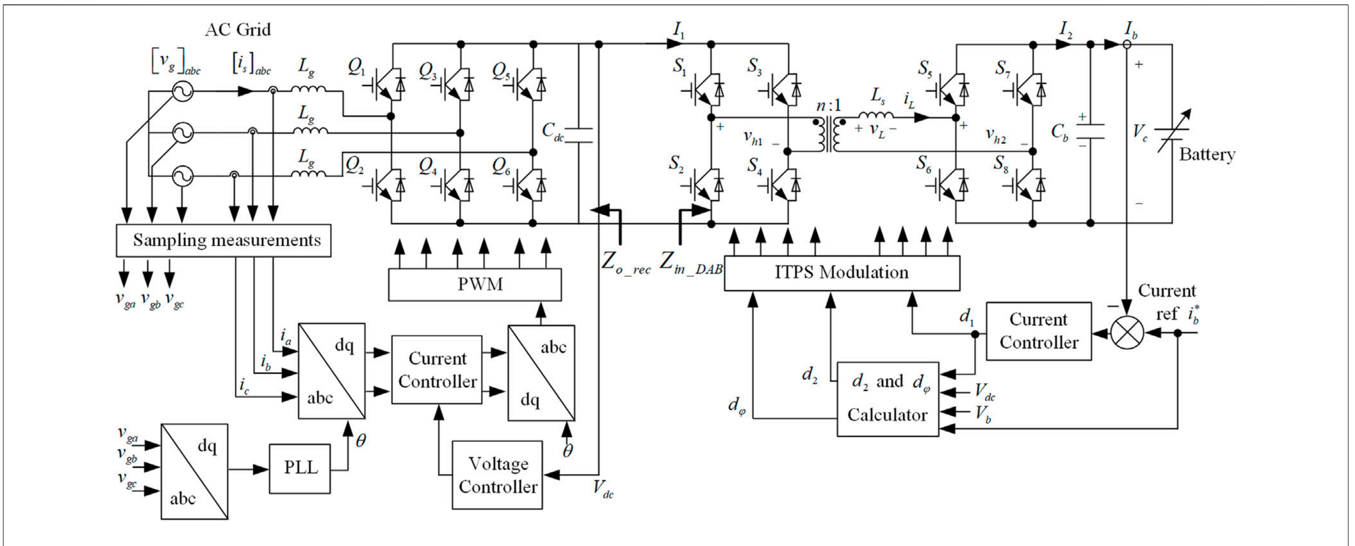

FIGURE 4 | The control block diagram of the two-stage AC-DC-DC converter.

converter to current-controlled sub-converter. Considering the control arrangement in **Figure 4**, the stability of the two-stage converter in battery charging mode, i.e., the power is transferred from the rectifier to the DAB converter, should be analyzed. Hence, the input impedance of the DAB converter in the battery charging mode are derived in the following section.

2.3 Output Impedance of the AC-DC Rectifiers

The performance and control of the three-phase AC-DC rectifier have been well studied in the existing literature. The derivation process of the small signal model of the rectifier which can be found in Literature Twining and Holmes (2003) is omitted here for conciseness. The output impedance Z_{o_rec} of the rectifier can be expressed as:

$$Z_{o\_rec} = \frac{-2\left(sL_g - V_{dc}G_{ci}\right)}{2s^2 C_{dc}L_g - 2sC_{dc}V_{dc}G_{ci} + 3\left(D_d^2 + D_q^2\right) - 3G_{ci}D_d I_{Ld}} \tag{5}$$

where C_{dc} is the dc-link capacitance; L_g is the input filter inductance of the rectifier; G_{ci} is the controller of the rectifier; I_{Ld} is the d-axis component of the inductor current; D_d and D_q denote the d- and q-axes components of the duty ratio of the rectifier, respectively.

3 IMPEDANCE MODELING OF CTPS-DAB CONVERTERS

3.1 Small Signal Impedance Modeling

The impedance model of the CTPS-DAB converter is derived first based on the simplified circuit shown in **Figure 5**. The voltage-controlled AC-DC rectifier can be regarded as a DC voltage source. R_b is the equivalent load of the battery in the charging

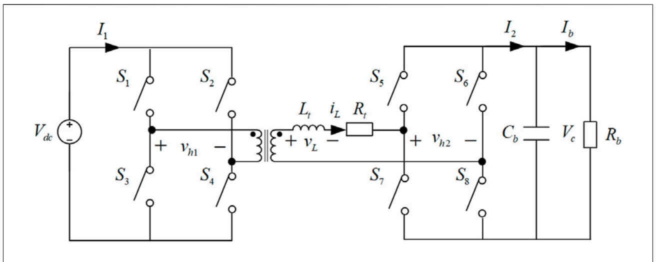

FIGURE 5 | The simplified circuit of the DAB converter.

operation mode. R_t is the winding resistance of the transformer. The capacitor voltage v_c and the inductor current i_L are taken as the state variables. The state equations of the CTPS-DAB converter can be expressed as:

$$L_t\frac{di_L}{dt} = \frac{v_{h1}}{n} - v_{h2} - R_t i_L = \frac{g_1 v_{dc}}{n} - g_2 v_c - R_t i_L \tag{6}$$

$$C_b\frac{dv_c}{dt} = i_2 - i_b = g_2 i_L - \frac{v_c}{R_b} \tag{7}$$

where g_1 and g_2 are the switching functions of the two H-bridges at the primary and secondary sides of the transformer. They can be expressed as follows according to **Figure 3**.

$$g_1(t) = \begin{cases} 1, & [t_1, t_3) \\ 0, & [t_0, t_1) \cup [t_3, t_4) \\ -1, & [t_4, t_6) \end{cases} \tag{8}$$

$$g_2(t) = \begin{cases} 1, & [t_2, t_4) \\ 0, & [t_1, t_2) \cup [t_4, t_5) \\ -1, & [t_0, t_1) \cup [t_5, t_6) \end{cases} \tag{9}$$

Due to the high-frequency ac link in the DAB converter, the generalized state-space averaging (GSSA) method is applied (Caliskan et al., 1999; Qin and Kimball 2012). The averages of the state variables and the switching functions are approximated by the sum of the index-0 and index-1 coefficient of their Fourier series. This leads to the following state-variable vector,

$$\mathbf{x} = \left[\langle v_c \rangle_0 \quad \langle v_c \rangle_1^R \quad \langle v_c \rangle_1^I \quad \langle i_L \rangle_0 \quad \langle i_L \rangle_1^R \quad \langle i_L \rangle_1^I \right]^T \tag{10}$$

where the subscripts denote the number of the coefficients of the Fourier series; the superscripts "R" and "I" mean the real and imaginary parts of the first coefficients, respectively. These rules apply in the whole paper.

In Literature Qin and Kimball (2012), the authors show that the dynamics of $\langle v_c \rangle_1^R$, $\langle v_c \rangle_1^I$ and $\langle i_L \rangle_0$ are decoupled from the rest of the system. Hence, the state-variable vector is reduced to $\mathbf{x} = [\, \langle v_c \rangle_0 \quad \langle i_L \rangle_1^R \quad \langle i_L \rangle_1^I \,]^T$.

Taking the Fourier series of the switching functions, the zeroth coefficients $\langle g_1 \rangle_0 = \langle g_2 \rangle_0 = 0$ due to the symmetry of the operation waveforms. The complex number index-1 coefficients of $g_1(t)$ and $g_2(t)$ are given by,

$$\langle g_1 \rangle_1^R = -\frac{\sin(d_1\pi)}{\pi} \tag{11}$$

$$\langle g_1 \rangle_1^I = -\frac{1+\cos(d_1\pi)}{\pi} \tag{12}$$

$$\langle g_2 \rangle_1^R = -\frac{\sin(d_1\pi) + \sin(d_1+d_2)\pi}{\pi} \tag{13}$$

$$\langle g_2 \rangle_1^I = -\frac{\cos(d_1\pi) + \cos(d_1+d_2)\pi}{\pi} \tag{14}$$

The resulting GSSA state equations can be obtained as **Eq. 15**. The output vector $\mathbf{y} = [\, i_1 \quad i_b \,]^T$ can be expressed as **Eq. 16**.

$$\dot{\mathbf{x}} = \begin{bmatrix} -\frac{1}{C_b R_b} & \frac{2\langle g_2 \rangle_1^R}{C_b} & \frac{2\langle g_2 \rangle_1^I}{C_b} \\ -\frac{\langle g_2 \rangle_1^R}{L_t} & -\frac{R_t}{L_t} & \omega_s \\ -\frac{\langle g_2 \rangle_1^I}{L_t} & -\omega_s & -\frac{R_t}{L_t} \end{bmatrix} \mathbf{x} + \begin{bmatrix} 0 \\ \frac{\langle g_1 \rangle_1^R}{nL_t} \\ \frac{\langle g_1 \rangle_1^I}{nL_t} \end{bmatrix} \langle v_{dc} \rangle_0 \tag{15}$$

where $\dot{\mathbf{x}}$ is the derivative of the state vector.

$$\mathbf{y} = \begin{bmatrix} 0 & 2n\langle g_1 \rangle_1^R & 2n\langle g_1 \rangle_1^I \\ \frac{1}{R_b} & 0 & 0 \end{bmatrix} \mathbf{x} + \begin{bmatrix} 0 \\ 0 \end{bmatrix} \langle v_{dc} \rangle_0 \tag{16}$$

The equilibrium point can be derived by solving $\dot{x} = 0$. The small signal model can be obtained by perturbating the input variables around the equilibrium point. Note that in this paper, for the variable x, its small signal notation is $\hat{x}$ and its steady state value is denoted by the uppercase letter X. d_2 is calculated from **Eq. 2**. Substituting **Eq. 2** into **Eqs 15**, **16**, d_2 is replaced by d_1, v_c and v_{dc}. The input vector is thus given by,

$$\hat{\mathbf{u}} = \left[\hat{v}_{dc} \quad \hat{d}_1 \right] \tag{17}$$

The open-loop small signal model of the CTPS-DAB converter is expressed in **Eq. 18**.

$$\begin{aligned} \dot{\hat{\mathbf{x}}} &= \mathbf{A}\hat{\mathbf{x}} + \mathbf{B}\hat{\mathbf{u}} \\ \hat{\mathbf{y}} &= \mathbf{C}\hat{\mathbf{x}} + \mathbf{D}\hat{\mathbf{u}} \end{aligned} \tag{18}$$

where $\mathbf{A}$, $\mathbf{B}$, $\mathbf{C}$, $\mathbf{D}$ are system matrix:

$$\mathbf{A} = \begin{bmatrix} A_{11} & \frac{2\langle g_2 \rangle_1^R}{C_b} & \frac{2\langle g_2 \rangle_1^I}{C_b} \\ A_{21} & -\frac{R_t}{L_t} & \omega_s \\ A_{31} & -\omega_s & -\frac{R_t}{L_t} \end{bmatrix} \tag{18a}$$

$$\mathbf{B} = \begin{bmatrix} B_{11} & B_{12} \\ B_{21} & B_{22} \\ B_{31} & B_{32} \end{bmatrix} \tag{18b}$$

$$\mathbf{C} = \begin{bmatrix} 0 & 2n\langle g_1 \rangle_1^R & 2n\langle g_1 \rangle_1^I \\ \frac{1}{R_b} & 0 & 0 \end{bmatrix} \tag{18c}$$

$$\mathbf{D} = \begin{bmatrix} 0 & 2\left(I_L^R \frac{\partial \langle g_1 \rangle_1^R}{\partial d_1} + I_L^I \frac{\partial \langle g_1 \rangle_1^I}{\partial d_1} \right) \\ 0 & 0 \end{bmatrix} \tag{18d}$$

$$A_{11} = -\frac{1}{C_b R_b} + \frac{2}{C_b}\left(I_L^R \frac{\partial \langle g_2 \rangle_1^R}{\partial v_c} + I_L^I \frac{\partial \langle g_2 \rangle_1^I}{\partial v_c} \right) \tag{18e}$$

$$A_{21} = -\frac{\langle g_2 \rangle_1^R}{L_s} - \frac{V_c}{L_s}\frac{\partial \langle g_2 \rangle_1^R}{\partial v_c} \tag{18f}$$

$$A_{31} = -\frac{\langle g_2 \rangle_1^I}{L_t} - \frac{V_c}{L_t}\frac{\partial \langle g_2 \rangle_1^I}{\partial v_c} \tag{18g}$$

$$B_{11} = \frac{2}{C_b}\left(I_L^R \frac{\partial \langle g_2 \rangle_1^R}{\partial v_{dc}} + I_L^I \frac{\partial \langle g_2 \rangle_1^I}{\partial v_{dc}} \right) \tag{18h}$$

$$B_{12} = \frac{2}{C_b}\left(I_L^R \frac{\partial \langle g_2 \rangle_1^R}{\partial d_1} + I_L^I \frac{\partial \langle g_2 \rangle_1^I}{\partial d_1} \right) \tag{18i}$$

$$B_{21} = \frac{\langle g_1 \rangle_1^R}{L_t} - \frac{V_c}{L_t}\frac{\partial \langle g_2 \rangle_1^R}{\partial v_{dc}} \tag{18j}$$

$$B_{22} = -\frac{V_c}{L_t}\frac{\partial \langle g_2 \rangle_1^R}{\partial d_1} + \frac{V_{dc}}{nL_t}\frac{\partial \langle g_1 \rangle_1^R}{\partial d_1} \tag{18k}$$

$$B_{31} = \frac{\langle g_1 \rangle_1^I}{L_t} - \frac{V_c}{L_t}\frac{\partial \langle g_2 \rangle_1^I}{\partial v_{dc}} \tag{18l}$$

$$B_{32} = -\frac{V_c}{L_t}\frac{\partial \langle g_2 \rangle_1^I}{\partial d_1} + \frac{V_{dc}}{nL_t}\frac{\partial \langle g_1 \rangle_1^I}{\partial d_1} \tag{18m}$$

The partial derivatives are given by,

$$\frac{\partial \langle g_1 \rangle_1^R}{\partial d_1} = -\cos(D_1\pi) \tag{19a}$$

$$\frac{\partial \langle g_1 \rangle_1^I}{\partial d_1} = \sin(D_1\pi) \tag{19b}$$

$$\frac{\partial \langle g_2 \rangle_1^R}{\partial d_1} = -\cos(D_1\pi) - (1+k)\cos((D_1+D_2)\pi) \tag{19c}$$

$$\frac{\partial \langle g_2 \rangle_1^I}{\partial d_1} = \sin(D_1\pi) + (1+k)\sin((D_1+D_2)\pi) \tag{19d}$$

$$\frac{\partial \langle g_2 \rangle_1^R}{\partial v_{dc}} = -\frac{D_1 - 1}{nV_c}\cos((D_1+D_2)\pi) \tag{19e}$$

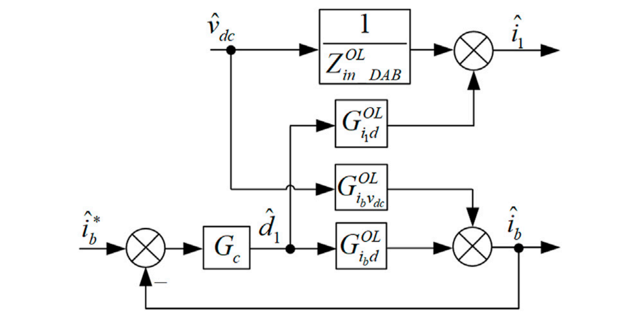

FIGURE 6 | Control block of the DAB converter.

$$\frac{\partial\langle g_2\rangle_1^R}{\partial v_c} = k\frac{D_1-1}{V_c}\cos\left((D_1+D_2)\pi\right) \tag{19f}$$

$$\frac{\partial\langle g_2\rangle_1^I}{\partial v_{dc}} = \frac{D_1-1}{nV_c}\sin\left((D_1+D_2)\pi\right) \tag{19g}$$

$$\frac{\partial\langle g_2\rangle_1^I}{\partial v_c} = -k\frac{D_1-1}{V_c}\sin\left((D_1+D_2)\pi\right) \tag{19h}$$

The open-loop transfer functions can be obtained as **Eqs 20a–d** by solving the open-loop small signal model Eq. 18 using MATLAB.

$$Z_{in\_DAB}^{OL} = \frac{(s-A_{11})\left[\left(s+\frac{R_t}{L_t}\right)^2+\omega_s^2\right]-\frac{2\langle g_2\rangle_1^R}{C_b}\left[A_{21}\left(s+\frac{R_t}{L_t}\right)+A_{31}\omega_s\right]-\frac{2\langle g_2\rangle_1^I}{C_b}\left[A_{31}\left(s+\frac{R_t}{L_t}\right)-A_{21}\omega_s\right]}{\left\{\begin{array}{l}\left[\left(2n\langle g_1\rangle_1^R A_{21}+2n\langle g_1\rangle_1^I A_{31}\right)s+2n\langle g_1\rangle_1^R\left(A_{21}\frac{R_t}{L_t}+A_{31}\omega_s\right)+2n\langle g_1\rangle_1^I\left(A_{31}\frac{R_t}{L_t}-A_{21}\omega_s\right)\right]B_{11}\\+\left[2n\langle g_1\rangle_1^R\left(s^2-\left(A_{11}-\frac{R_t}{L_t}\right)s-A_{11}\frac{R_t}{L_t}-\frac{2\langle g_2\rangle_1^I}{C_b}A_{31}\right)+2n\langle g_1\rangle_1^I\left(-\omega_s s+A_{11}\omega_s+\frac{2\langle g_2\rangle_1^I}{C_b}A_{31}\right)\right]B_{21}\\+\left[2n\langle g_1\rangle_1^R\left(\omega_s s-A_{11}\omega_s+\frac{2\langle g_2\rangle_1^I}{C_b}A_{21}\right)+2n\langle g_1\rangle_1^I\left(s^2-\left(A_{11}-\frac{R_t}{L_t}\right)s-A_{11}\frac{R_t}{L_t}-\frac{2\langle g_2\rangle_1^R}{C_b}A_{21}\right)\right]B_{31}\end{array}\right\}} \tag{20a}$$

$$G_{i_1d_1} = \frac{\left\{\begin{array}{l}\left[\left(2n\langle g_1\rangle_1^R A_{21}+2n\langle g_1\rangle_1^I A_{31}\right)s+2n\langle g_1\rangle_1^R\left(A_{21}\frac{R_t}{L_t}+A_{31}\omega_s\right)+2n\langle g_1\rangle_1^I\left(A_{31}\frac{R_t}{L_t}-A_{21}\omega_s\right)\right]B_{12}\\+\left[2n\langle g_1\rangle_1^R\left(s^2-\left(A_{11}-\frac{R_t}{L_t}\right)s-A_{11}\frac{R_t}{L_t}-\frac{2\langle g_2\rangle_1^I}{C_b}A_{31}\right)+2n\langle g_1\rangle_1^I\left(-\omega_s s+A_{11}\omega_s+\frac{2\langle g_2\rangle_1^I}{C_b}A_{31}\right)\right]B_{22}\\+\left[2n\langle g_1\rangle_1^R\left(\omega_s s-A_{11}\omega_s+\frac{2\langle g_2\rangle_1^I}{C_b}A_{21}\right)+2n\langle g_1\rangle_1^I\left(s^2-\left(A_{11}-\frac{R_t}{L_t}\right)s-A_{11}\frac{R_t}{L_t}-\frac{2\langle g_2\rangle_1^R}{C_b}A_{21}\right)\right]B_{32}\end{array}\right\}}{(s-A_{11})\left[\left(s+\frac{R_t}{L_t}\right)^2+\omega_s^2\right]-\frac{2\langle g_2\rangle_1^R}{C_b}\left[A_{21}\left(s+\frac{R_t}{L_t}\right)+A_{31}\omega_s\right]-\frac{2\langle g_2\rangle_1^I}{C_b}\left[A_{31}\left(s+\frac{R_t}{L_t}\right)-A_{21}\omega_s\right]} \tag{20b}$$

$$G_{i_bv_{dc}} = \frac{C_b\left[\left(s+\frac{R_t}{L_t}\right)^2+\omega_s^2\right]B_{11}+2\langle g_2\rangle_1^R\left(s+\frac{R_t}{L_t}\right)B_{21}-2\langle g_2\rangle_1^I\omega_s B_{21}+2\langle g_2\rangle_1^R\omega_s B_{31}+2\langle g_2\rangle_1^I\left(s+\frac{R_t}{L_t}\right)B_{31}}{R_bC_b(s-A_{11})\left[\left(s+\frac{R_t}{L_t}\right)^2+\omega_s^2\right]-2R_b\langle g_2\rangle_1^R\left[A_{21}\left(s+\frac{R_t}{L_t}\right)+A_{31}\omega_s\right]-2R_b\langle g_2\rangle_1^I\left[A_{31}\left(s+\frac{R_t}{L_t}\right)-A_{21}\omega_s\right]} \tag{20c}$$

$$G_{i_bd_1} = \frac{C_b\left[\left(s+\frac{R_t}{L_t}\right)^2+\omega_s^2\right]B_{12}+2\langle g_2\rangle_1^R\left(s+\frac{R_t}{L_t}\right)B_{22}-2\langle g_2\rangle_1^I\omega_s B_{22}+2\langle g_2\rangle_1^R\omega_s B_{32}+2\langle g_2\rangle_1^I\left(s+\frac{R_t}{L_t}\right)B_{32}}{R_bC_b(s-A_{11})\left[\left(s+\frac{R_t}{L_t}\right)^2+\omega_s^2\right]-2R_b\langle g_2\rangle_1^R\left[A_{21}\left(s+\frac{R_t}{L_t}\right)+A_{31}\omega_s\right]-2R_b\langle g_2\rangle_1^I\left[A_{31}\left(s+\frac{R_t}{L_t}\right)-A_{21}\omega_s\right]} \tag{20d}$$

The battery current is measured in the control loop of the DAB converter. The control block diagram is shown in **Figure 6**. G_c is the controller of the DAB converter based on PI structure. From **Figure 6**, the closed-loop input impedance Z_{in_DAB} can be obtained in **Eq. 21** based on Mason's gain formula (Nise 2007).

$$\frac{1}{Z_{in\_DAB}} = \frac{\hat{i}_1}{\hat{v}_{dc}} = \frac{1}{Z_{in\_DAB}^{OL}} - \frac{G_{i_bv_{dc}}^{OL}G_cG_{i_1d_1}^{OL}}{1+T} = \frac{(1+T)-G_{i_bv_{dc}}^{OL}G_cG_{i_1d_1}^{OL}Z_{in\_DAB}^{OL}}{(1+T)Z_{in\_DAB}^{OL}} \tag{21}$$

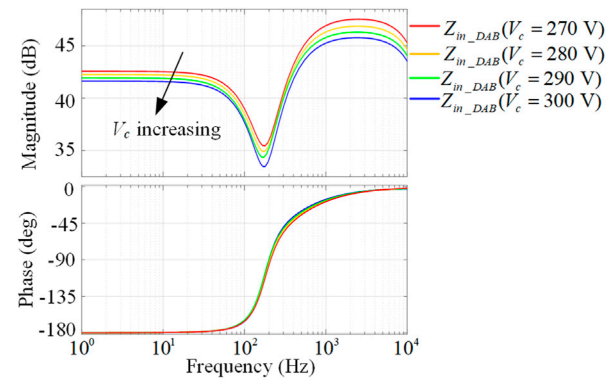

FIGURE 7 | Bode plots of Z_{in_DAB} with different V_c.

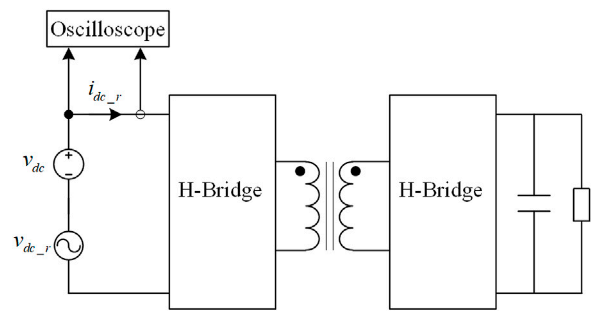

FIGURE 8 | Measurement of Z_{in_DAB}.

where T is the loop gain of the DAB converter and $T = G_cG_{i_bd_1}^{OL}$.

And Z_{in_DAB} can be further simplified as **Eq. 22**.

$$Z_{in\_DAB} = \frac{(1+T)Z_{in\_DAB}^{OL}}{(1+T)-G_{i_bv_{dc}}^{OL}G_cG_{i_1d_1}^{OL}Z_{in\_DAB}^{OL}} \tag{22}$$

Eq. 22 can be used to determine the closed-loop input impedance of DAB converters around a certain operating point when the battery voltage changes V_c due to the state-of-charge variations.

It should be mentioned that the battery voltage varies between 270 and 300 V due to the SOC change. Therefore, it is meaningful to investigate the influences of the battery voltage on the DAB input impedance models. **Figure 7** shows the bode plots of a set of linearized input impedance models around four different operating points, when V_c is incrementally changed from 270 to 300 V. The magnitude of Z_{in_DAB} is slightly decreased with the increase of V_c, although the phase angles of Z_{in_DAB} are almost the same. According to the Middlebrook criterion, the stability of the two-stage converter requires Z_{in_DAB} larger than Z_{o_rec}. The unstable problem of the two-stage converter most likely happens when the input impedance of the DAB converter presents the lowest magnitude. Therefore, to ensure the stability within the whole operation range, the stability of the

TABLE 2 | Circuit parameters of the two-stage converter.

Parameter	Value	Parameter	Value
Equivalent load resistance R_b	25 Ω	DC bus voltage V_{dc}	660 V
The turns ratio of the transformer n	2	DC bus filter capacitance C_{dc}	2,000 µF
DC side output voltage V_c	300 V	Proportional coefficient of the DC voltage controller for the AC-DC rectifier K_{pv}	10
The DC side output filter capacitance C_b	1,000 µF	Integral coefficient of the DC voltage controller for the AC-DC rectifier K_{iv}	150
Capacitance equivalent series resistance R_c	0.8 Ω	Proportional coefficient of the current controller for the AC-DC rectifier K_{pi}	4
DC inductor L_t	100 µH	Integral coefficient of the current controller for the AC-DC rectifier K_{ii}	100
Winding resistance R_t	0.4 Ω	Filter inductor of the AC-DC rectifier L_g	0.002 H
Proportional coefficient of the current controller for the DAB converter K_p	1.2	Parasitic resistance of the filter inductor R_g	0.16
Integral coefficient of the current controller for the DAB converter K_i	160	Switching frequency of the DAB converter f_s	20 kHz

two-stage converter should be assessed when the battery voltage is 300 V.

3.2 Validation of Input Impedance Models

The validity of the developed input impedance model is verified using fully detailed simulation in MATLAB/Simulink environment. The measurement of Z_{in_DAB} is shown in **Figure 8**. Similar impedance measurement methods have been successfully applied in (Huang et al., 2009; Rygg and Molinas 2017). The parameters of the two-stage converter are shown in **Table 2**. The deadtime of the switches and the sampling period are set as 0.2 and 250 µs, respectively. The simulation time step is fixed to 0.1 µs. The AC-DC rectifier is replaced by a controllable ripple voltage source connected in series with a 660 V DC voltage source. A sinusoidal perturbation is generated at the DC bus, which is superimposed on steady-state DC voltage as the ripple voltage, v_{dc_r}. The magnitude of v_{dc_r} is set to 1 and the frequency of v_{dc_r} varies logarithmically from 2 Hz to 10 kHz. The corresponding DC bus currents are also measured. The magnitude and phase of the current ripple, i_{dc_r}, are extracted by FFT analysis at each frequency. The impedance of the DAB converter at different frequencies can be calculated by **Eq. 23**.

$$Z_{in\_DAB} = \frac{v_{dc\_r}}{i_{dc\_r}} \tag{23}$$

The bode plots of Z_{in_DAB} with measured values and model predictive values are shown in **Figure 9**. The impedance model predicted results match well with the measured results from the low frequencies up to the half of the switching frequency f_s. Therefore, the developed impedance model can provide fairly accurate prediction for the input impedance of the CTPS-DAB converter. Furthermore, Z_{in_DAB} shows negative resistance characteristics at the low frequencies. Moreover, the magnitude of Z_{in_DAB} is reduced at about 200 Hz. This is the potential threat for stability consideration of the two-stage converter. If the magnitude of Z_{in_DAB} is lower than that of Z_{o_rec} within the low frequency range, the two-stage converter will be unstable. Hence, it is necessary to increase the minimum magnitude value of Z_{in_DAB}. Since the DAB converter circuit parameters are included in the impedance model, the most straightforward method to modify the DAB input impedance is to optimize the DAB circuit parameters. Thus, the effects of the DAB converter circuit parameters on the stability of the two-stage converter should be analyzed.

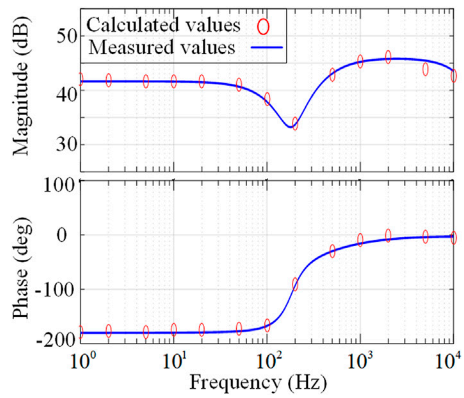

FIGURE 9 | Bode plots of the input impedances of the DAB converters. 'o' represents the measured values.

4 STABILITY-ORIENTED OPTIMIZATION OF CIRCUIT PARAMETERS

For the stability consideration, the magnitude intersection between Z_{in_DAB} and Z_{o_rec} should be avoided. The minimum value of Z_{in_DAB} should be designed in the range above the peak value of Z_{o_rec}. From **Eq. 18** to **Eq. 22**, the inductor L_s and DC side output filter capacitor C_b are included in the impedance model Z_{in_DAB}. Therefore, to improve the stability of the two-stage converter, the most effective and easiest method is to optimize the value of L_s and C_b.

4.1 Stability Improvement by Optimization of L_s

To analyze the effects of L_s on the minimum of Z_{in_DAB}, **Figure 10A** shows the bode plots of Z_{in_DAB} with different values of L_s. The rest of the circuit parameters are listed in **Table 2**. The minimum of Z_{in_DAB} increases with the reduction of L_s. When L_s is 200 µH or 100 µH, Z_{in_DAB} intersects with Z_{o_rec}, indicating that the two-stage converter

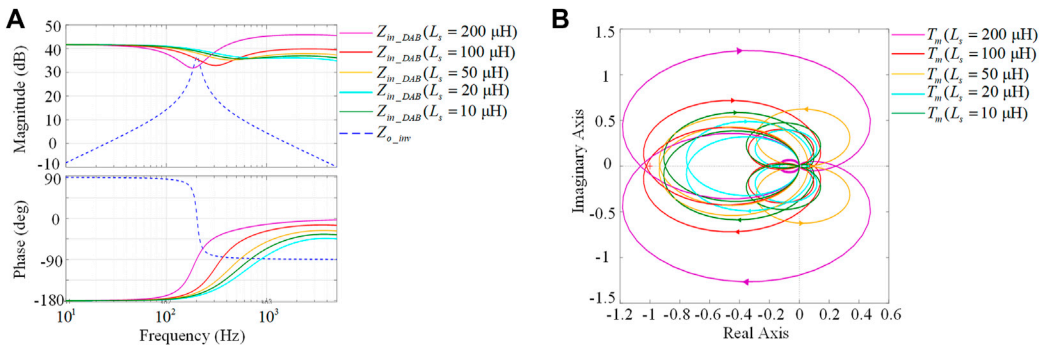

FIGURE 10 | (A) Bode plots and **(B)** Nyquist plots of T_m with decreased L_s.

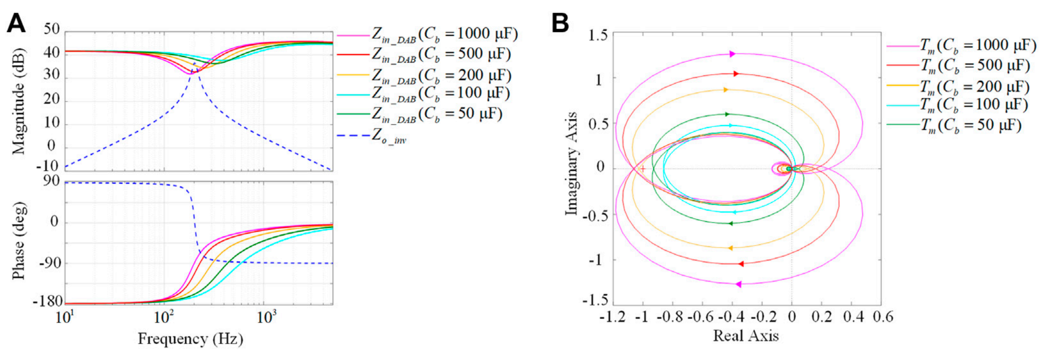

FIGURE 11 | (A) Bode plots and **(B)** Nyquist plots of T_m with decreased C_b.

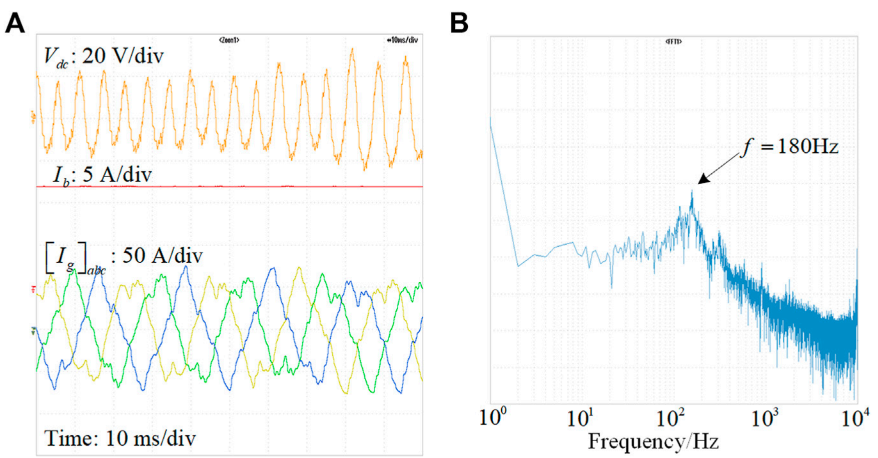

FIGURE 12 | (A) Waveforms of the two-stage converter with original parameters; **(B)** FFT analysis of V_{dc} with original parameters.

is unstable. However, for L_s smaller than 50 μH, the minimum value of Z_{in_DAB} is larger than the magnitude of Z_{o_rec} within all operation frequencies. According to the Middlebrook criterion, the two-stage converter is stable under such conditions.

The influences of L_s on the stability of two-stage converter can be further illustrated by the Nyquist plots of T_m shown in **Figure 10B**. The trajectory of T_m encircles the critical point (−1, 0) when L_s is 200 μH or 100 μH, suggesting that there is a right-hand plane pole in the s-plane. The two-stage converter is hence unstable with these two inductors. And the stability of the two-stage converter can be improved by reducing the value of L_s. As seen from **Figure 10B**, with the reduction of L_s, the gain margin and phase margin are both

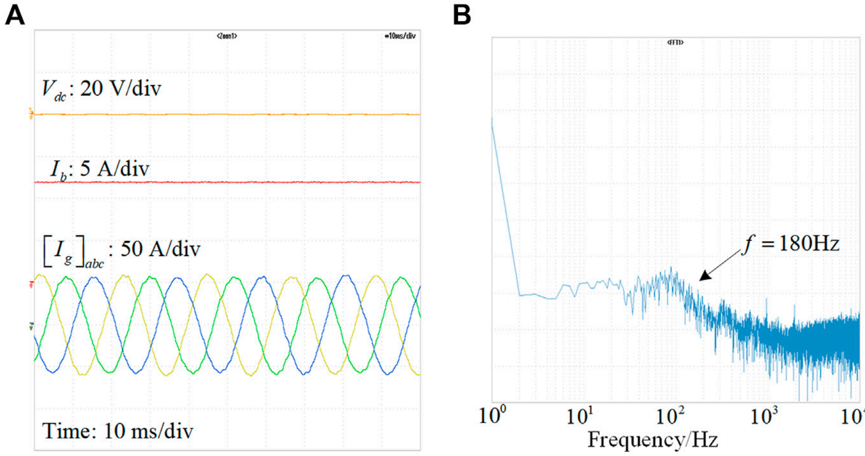

FIGURE 13 | (A) Waveforms of the two-stage converter with reduced L_s; **(B)** FFT analysis of V_{dc} with reduced L_s.

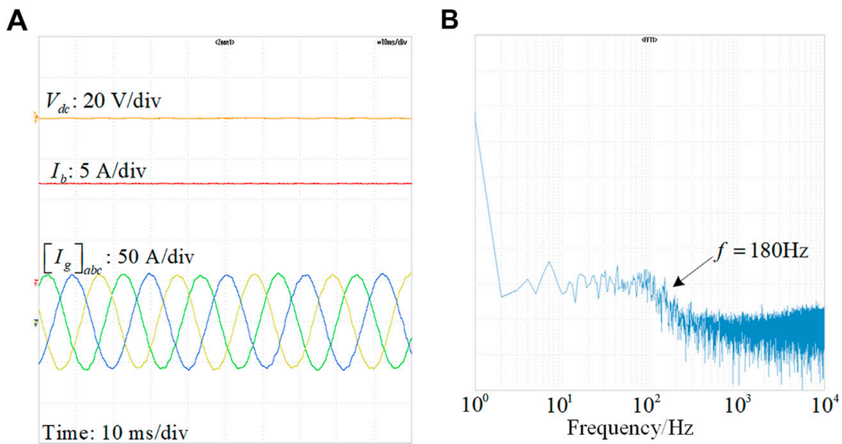

FIGURE 14 | (A) Waveforms of the two-stage converter with reduced C_b; **(B)** FFT analysis of V_{dc} with reduced C_b.

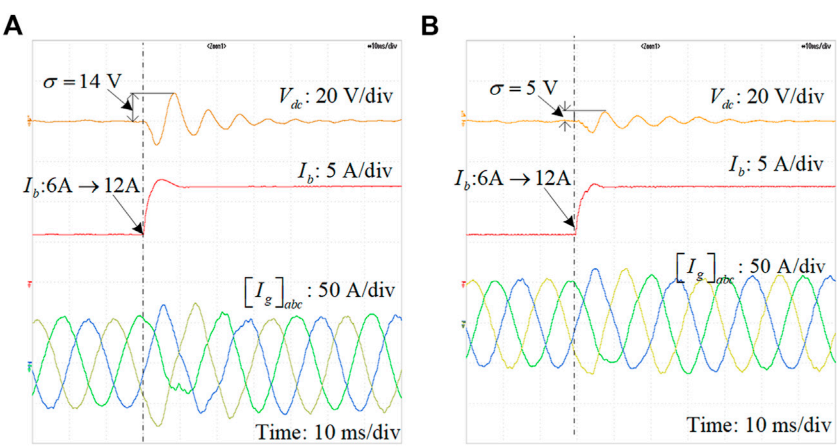

FIGURE 15 | (A) Dynamic performance of the two-stage converter with reduced L_s; **(B)** dynamic performance of the two-stage converter with reduced C_b.

increased. When L_s is smaller than 50 μH, the trajectory of T_m no longer encircles (−1, 0) anymore. This can also be deduced from **Figure 10A**, where the minimum value of Z_{in_DAB} is gradually increased with the reduction of L_s. Therefore, for improving the stability of the two-stage converter, a relatively small value of L_s is preferred, although the other factors such as power transfer ability should also be considered.

4.2 Stability Improvement by Optimization of C_b

Similarly, to analyze the influences of C_b on the stability of the two-stage converter, a set of C_b are selected. The relationship between the value of C_b and the minimum magnitude of Z_{in_DAB} is shown in **Figure 11A**. The minimum magnitude of Z_{in_DAB} keeps decreasing with the reduction of C_b. From **Figure 11A**, when C_b is larger than 200 μF, Z_{in_DAB} and Z_{o_rec} intersect with each other, which can cause the unstable problem to the two-stage converter.

The effects of C_b on system stability are further illustrated by the Nyquist plots shown in **Figure 11B**. From **Figure 11B**, When C_b is larger than 200 μF, the trajectory of T_m encircles the point (−1, 0). This indicates that the two-stage converter cannot maintain its stability. However, with C_b decreasing from 1,000 μF to 50 μF, the gain margin and the phase margin of the two-stage converter increase gradually. And the two-stage converter is stable when C_b is smaller than 100 μF. The conclusion that can be drawn from the Nyquist plot together with the bode plots is that a relatively small value of C_b is good for the stability consideration.

5 EXPERIMENTAL RESULTS AND DISCUSSION

The hardware-in-the-loop (HIL) experimental system has been proven to be an effective method for stability analysis of power electronic converters (Zhang et al., 2018). To verify the theoretical analysis, the stability of the two-stage converter is tested based on the OPAL-RT based HIL experimental system. The parameters of the experimental system are shown in **Table 2**. It should be noted that the waveform of V_{dc} in **Figures 12–15** are only its AC components to show the stability.

Figure 12A shows the waveforms of the two-stage converter with original circuit parameters (L_s = 200 μH, C_b = 1,000 μF). As seen, the oscillation at V_{dc} can be found. Moreover, the oscillating frequency is around 180 Hz, which is consistent with the prediction of the bode plot in **Figure 10A**. The instable problem of the two-stage converter can be more visualized from the FFT spectra of V_{dc} shown in **Figure 12B**. The amplitude of the 180 Hz harmonic component is significant. This is the root cause of the waveform oscillation.

Considering the effects of L_s on the minimum magnitude of Z_{in_DAB}, L_s should be reduced to improve the stability. **Figure 13A** shows the waveforms of the two-stage converter with reduced L_s = 50 μH and other parameters being unchanged. The oscillation at V_{dc} is mitigated as expected. This is because the minimum magnitude of Z_{in_DAB} is increased and there is no intersection between Z_{in_DAB} and Z_{o_rec} as shown in **Figure 10A**. It can be also observed from the FFT spectra of V_{dc} in **Figure 13B** that the quantities of the 180 Hz harmonic response are suppressed.

Similarly, according to the above-mentioned analysis, C_b should be reduced to for stability consideration. **Figure 14A** shows the waveforms of the two-stage converter with C_b = 100 μF and other parameters being constant. The waveforms show that the two-stage converter is stable with reduced C_b. According to FFT spectra of V_{dc} in **Figure 14B**, the 180 Hz harmonic response is also greatly suppressed.

The dynamic performances of the two-stage converter with reduced L_s and C_b are also tested and shown in **Figure 15**. When I_b steps up from 6 to 12 A, V_{dc} can be stabilized with reduced L_s or C_b after a short transient period. However, when reduced L_s is applied, the overshoot of V_{dc} is about 14 V. When reduced C_b is applied, the overshoot of V_{dc} is only about 5 V.

Hence, the stability of the two-stage converter can be improved by optimizing L_s or C_b. Furthermore, the dynamic performance of the two-stage converter with reduced C_b is better than that of the two-stage converter with reduced L_s according to the experimental waveforms.

6 CONCLUSION

The full-order impedance model of the CTPS based DAB converter has been derived in this paper. The developed impedance model can fully represent the dynamics of the ac conversion stage of the DAB converters. Based on the developed impedance model, the stability of two-stage converter has been analyzed. Furthermore, the effects of the DAB circuit parameters on the stability of the two-stage converter have been presented and analyzed. The design of the DAB circuit parameters is revisited. The stability-oriented optimization guideline of circuit parameters is provided for the DAB converter. The stability of the two-stage converter can be improved by reducing the leakage inductance or the DC side output filter capacitance of the DAB converter.

DATA AVAILABILITY STATEMENT

The original contributions presented in the study are included in the article/Supplementary Material, further inquiries can be directed to the corresponding authors.

AUTHOR CONTRIBUTIONS

FF contributed to the conception of the study and wrote the manuscript; JF performed the data analyses; HG contributed to analysis and manuscript preparation. UM and LW performed the experiment.

FUNDING

This research was funded by the Special project for marine economy development of Guangdong Province [GDNRC(2022)31], Guangzhou Municipal Science and

Technology Bureau (Grant No. 2021020 21161), National Natural Science Foundation of China (Grant No. 52101342), Key-Area Research and Development Program of Guangdong Province (Grant No. 2021B0202070002), and Natural Science Foundation of Guangdong Province (Grant No. 2022A1515010792), Shandong University Distinguished Young Scholars Project grant number 31400012002201.

REFERENCES

Blaabjerg, F., Chen, Z., and Kjaer, S. B. (2004). Power Electronics as Efficient Interface in Dispersed Power Generation Systems. *IEEE Trans. Power Electron.* 19 (5), 1184–1194. doi:10.1109/tpel.2004.833453

Caliskan, V. A., Verghese, O. C., and Stankovic, A. M. (1999). Multifrequency Averaging of DC/DC Converters. *IEEE Trans. Power Electron.* 14 (1), 124–133. doi:10.1109/63.737600

Erika Twining, E., and Holmes, D. G. (2003). Grid Current Regulation of a Three-phase Voltage Source Inverter with an LCL Input Filter. *IEEE Trans. Power Electron.* 18 (3), 888–895. doi:10.1109/tpel.2003.810838

Feng, F., Zhang, X., Zhang, J., and Gooi, H. B. (2020). Stability Enhancement via Controller Optimization and Impedance Shaping for Dual Active Bridge-Based Energy Storage Systems. *IEEE Trans. Industrial Electron.* 68 (7), 5863–5874.

Hengsi Qin, H., and Kimball, J. W. (2012). Generalized Average Modeling of Dual Active Bridge DC-DC Converter. *IEEE Trans. Power Electron.* 27 (4), 2078–2084. doi:10.1109/tpel.2011.2165734

Huang, J., Corzine, K. A., and Belkhayat, M. (2009). Small-signal Impedance Measurement of Power-Electronics-Based AC Power Systems Using Line-To-Line Current Injection. *IEEE Trans. Power Electron.* 24 (2), 445–455. doi:10.1109/tpel.2008.2007212

Krismer, F., and Kolar, J. W. (2009). Accurate Small-Signal Model for the Digital Control of an Automotive Bidirectional Dual Active Bridge. *IEEE Trans. Power Electron.* 24 (12), 2756–2768. doi:10.1109/tpel.2009.2027904

Liu, F., Liu, J., Zhang, H., and Xue, D. (2014). Stability Issues of $Z + Z$ Type Cascade System in Hybrid Energy Storage System (HESS). *IEEE Trans. Power Electron.* 29 (11), 5846–5859. doi:10.1109/tpel.2013.2295259

Middlebrook, R., and Cuk, S. (1976). A General Unified Approach to Modelling Switching-Converter Power Stages. In Power Electronics Specialists Conference. IEEEIEEE. doi:10.1109/pesc.1976.7072895

Mueller, J. A., and Kimball, J. W. (2017). "Model-based Determination of Closed-Loop Input Impedance for Dual Active Bridge Converters," in *Applied Power Electronics Conference and Exposition (APEC), 2017 IEEE* (IEEE). doi:10.1109/apec.2017.7930824

Nise, N. S. (2007). *Control Systems Engineering, (With Cd)*. John Wiley & Sons.

Radwan, A. A. A., and Mohamed, Y. A.-R. I. (2012). Assessment and Mitigation of Interaction Dynamics in Hybrid AC/DC Distribution Generation Systems. *IEEE Trans. Smart Grid* 3 (3), 1382–1393. doi:10.1109/tsg.2012.2201965

Roggia, L., Schuch, L., Baggio, J. E., Rech, C., and Pinheiro, J. R. (2013). Integrated Full-Bridge-Forward DC-DC Converter for a Residential Microgrid Application. *IEEE Trans. Power Electron.* 28 (4), 1728–1740. doi:10.1109/tpel.2012.2214061

Rygg, A., and Molinas, M. (2017). Apparent Impedance Analysis: A Small-Signal Method for Stability Analysis of Power Electronic-Based Systems. *IEEE J. Emerg. Sel. Top. Power Electron.* 5 (4), 1474–1486. doi:10.1109/jestpe.2017.2729596

Sun, J. (2011). Impedance-based Stability Criterion for Grid-Connected Inverters. *IEEE Trans. Power Electron.* 26 (11), 3075–3078. doi:10.1109/tpel.2011.2136439

Tan, N. M. L., Abe, T., and Akagi, H. (2012). Design and Performance of a Bidirectional Isolated DC-DC Converter for a Battery Energy Storage System. *IEEE Trans. Power Electron.* 27 (3), 1237–1248. doi:10.1109/tpel.2011.2108317

Tian, Y., Loh, P. C., Chen, Z., Deng, F., and Hu, Y. (2016). Impedance Interactions in Bidirectional Cascaded Converter. *IET Power Electron.* 9 (13), 2482–2491. doi:10.1049/iet-pel.2015.0559

Tian, Y., Loh, P. C., Deng, F., Chen, Z., Sun, X., and Hu, Y. (2016). Impedance Coordinative Control for Cascaded Converter in Bidirectional Application. *IEEE Trans. Ind. Appl.* 52 (5), 4084–4095. doi:10.1109/tia.2016.2564359

Wen, B., Boroyevich, D., Burgos, R., Mattavelli, P., and Shen, Z. (2015). Small-Signal Stability Analysis of Three-phase AC Systems in the Presence of Constant Power Loads Based on Measured D-Q Frame Impedances. *IEEE Trans. Power Electron.* 30 (10), 5952–5963. doi:10.1109/tpel.2014.2378731

Wu, F., Feng, F., and Gooi, H. B. (2018). Cooperative Triple-Phase-Shift Control for Isolated DAB DC–DC Converter to Improve Current Characteristics. *IEEE Trans. Industrial Electron.* 66 (9), 7022–7031.

Wu, F., Li, X., Feng, F., and Gooi, H. B. (2015). Modified Cascaded Multilevel Grid-Connected Inverter to Enhance European Efficiency and Several Extended Topologies. *IEEE Trans. Ind. Inf.* 11 (6), 1358–1365. doi:10.1109/tii.2015.2486623

Wu, K., de Silva, C. W., and Dunford, W. G. (2012). Stability Analysis of Isolated Bidirectional Dual Active Full-Bridge DC-DC Converter with Triple Phase-Shift Control. *IEEE Trans. Power Electron.* 27 (4), 2007–2017. doi:10.1109/tpel.2011.2167243

Ye, Q., Mo, R., and Li, H. (2017). Low-frequency Resonance Suppression of a Dual Active Bridge (DAB) DC/DC Converter Enabled DC Microgrid with Constant Power Loads (CPLs) Based on Reduced-Order Impedance Models. *IEEE J. Emerg. Sel. Top. Power Electron.*

Zhang, X., Ruan, X., and Tse, C. K. (2015). Impedance-based Local Stability Criterion for Dc Distributed Power Systems. *IEEE Trans. Circuits Syst. I* 62 (3), 916–925. doi:10.1109/tcsi.2014.2373673

Zhang, X., Zhong, Q.-C., Kadirkamanathan, V., He, J., and Huang, J. (2018). Source-side Series-Virtual-Impedance Control to Improve the Cascaded System Stability and the Dynamic Performance of its Source Converter. *IEEE Trans. Power Electron.*

Zhao, C., Round, S. D., and Kolar, J. W. (2010). Full-order Averaging Modelling of Zero-Voltage-Switching Phase-Shift Bidirectional DC-DC Converters. *IET Pwr. Electr.* 3 (3), 400–410. doi:10.1049/iet-pel.2008.0208

Conflict of Interest: The authors declare that the research was conducted in the absence of any commercial or financial relationships that could be construed as a potential conflict of interest.